Supplement to: Challenges in reconstructing seasonally driven landslide motion from optical satellite data: insights from the Del Medio catchment, NW Argentina

Ariane Mueting[1], Laurane Charrier[2,3,4], and Bodo Bookhagen[1]

[1]Institute of Geosciences, University of Potsdam, Karl-Liebknecht-Str. 24-25, Potsdam-Golm 14476, Germany
[2]Univ. Grenoble Alpes, CNRS, IRD, INRAE, Grenoble-INP, Institut des Géosciences de l'Environnement (IGE, UMR 5001), 38000 Grenoble, France
[3]Univ. Grenoble Alpes, CNRS, Inria, Grenoble INP (Institute of Engineering Univ. Grenoble Alpes), LJK, 38000 Grenoble, France
[4]Meteo-France, CNRS, Univ. Grenoble Alpes, Univ. Toulouse, CNRM, Centre d'Etudes de la Neige, 38000 Grenoble, France

Correspondence: Ariane Mueting (mueting@uni-potsdam.de)

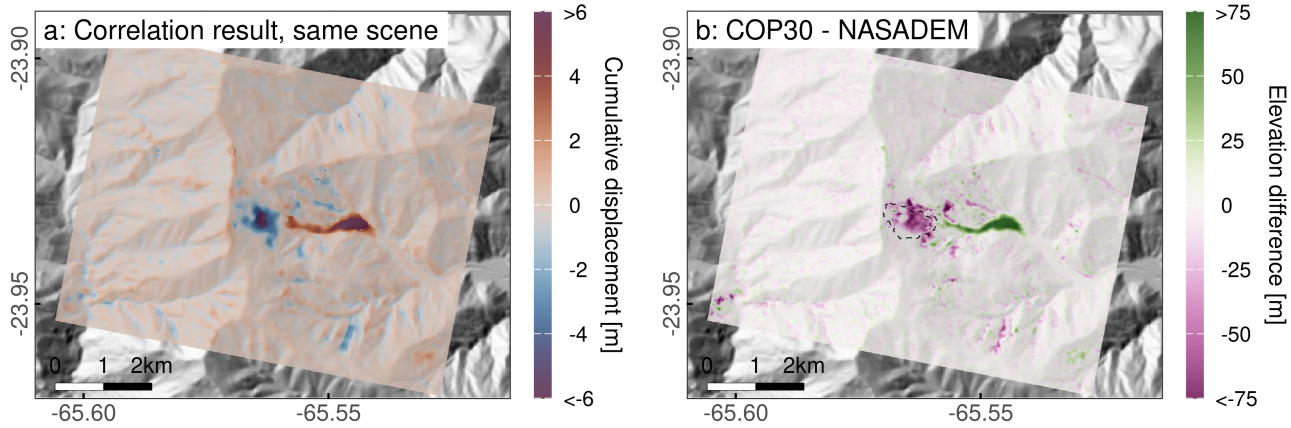

Figure S1. (a) Displacement field (east-west) calculated from an image pair of PlanetScope scenes. We correlated the exact same scene (id: 20210603_134145_29_2456), but once downloaded in 2023 (Mueting and Bookhagen, 2023) and once in 2025 for this study. The obtained displacement field should be zero, but clearly reflects the DEM difference between the NASADEM and Copernicus DEM, highlighting the elevation changes following the rockfall event in 2009 (b). This leads us to the assumption that the processing baseline was updated to consider the Copernicus DEM as a reference for orthorectification and L3B data was reprocessed. Constraining images to a common perspective, however, remains important because, since the acquisition of the Copernicus DEM, further elevation changes over the landslide have occurred. The moving surface identified in this study is outlined with a black dashed line in (b).

Scene ID	Acquisition Date	Instrument
LC08_L1TP_231077_20140228_20200911_02_T1	2014-02-28	Landsat-8
LC08_L1TP_231077_20140519_20200911_02_T1	2014-05-19	Landsat-8
LC08_L1TP_231077_20140722_20200911_02_T1	2014-07-22	Landsat-8
LC08_L1TP_231077_20141026_20200910_02_T1	2014-10-26	Landsat-8
LC08_L1TP_231077_20150404_20200909_02_T1	2015-04-04	Landsat-8
LC08_L1TP_231077_20150709_20200909_02_T1	2015-07-09	Landsat-8
LC08_L1TP_231077_20151013_20200908_02_T1	2015-10-13	Landsat-8
LC08_L1TP_231077_20160422_20200907_02_T1	2016-04-22	Landsat-8
LC08_L1TP_231077_20160812_20200906_02_T1	2016-08-12	Landsat-8
LC08_L1TP_231077_20161031_20200905_02_T1	2016-10-31	Landsat-8
LC08_L1TP_231077_20161218_20200905_02_T1	2016-12-18	Landsat-8
LC08_L1TP_231077_20170204_20200905_02_T1	2017-02-04	Landsat-8
LC08_L1TP_231077_20170425_20200904_02_T1	2017-04-25	Landsat-8
LC08_L1TP_231077_20170714_20200903_02_T1	2017-07-14	Landsat-8
LC08_L1TP_231077_20171002_20200903_02_T1	2017-10-02	Landsat-8
LC08_L1TP_231077_20171119_20200902_02_T1	2017-11-19	Landsat-8
LC08_L1TP_231077_20180428_20200901_02_T1	2018-04-28	Landsat-8
LC08_L1TP_231077_20180802_20200831_02_T1	2018-08-02	Landsat-8
LC08_L1TP_231077_20180919_20200830_02_T1	2018-09-19	Landsat-8
LC08_L1TP_231077_20181208_20200830_02_T1	2018-12-08	Landsat-8
LC08_L1TP_231077_20190330_20200829_02_T1	2019-03-30	Landsat-8
LC08_L1TP_231077_20190517_20200828_02_T1	2019-05-17	Landsat-8
LC08_L1TP_231077_20190704_20200827_02_T1	2019-07-04	Landsat-8
LC08_L1TP_231077_20190906_20200826_02_T1	2019-09-06	Landsat-8
LC08_L1TP_231077_20191024_20200825_02_T1	2019-10-24	Landsat-8
LC08_L1TP_231077_20200417_20200822_02_T1	2020-04-17	Landsat-8
LC08_L1TP_231077_20200722_20200911_02_T1	2020-07-22	Landsat-8
LC08_L1TP_231077_20201010_20201016_02_T1	2020-10-10	Landsat-8
LC08_L1TP_231077_20210130_20210302_02_T1	2021-01-30	Landsat-8
LC08_L1TP_231077_20210420_20210430_02_T1	2021-04-20	Landsat-8
LC08_L1TP_231077_20210725_20210803_02_T1	2021-07-25	Landsat-8
LC08_L1TP_231077_20211013_20211019_02_T1	2021-10-13	Landsat-8
LC08_L1TP_231077_20220407_20220412_02_T1	2022-04-07	Landsat-8
LC08_L1TP_231077_20220712_20220722_02_T1	2022-07-12	Landsat-8
LC08_L1TP_231077_20220914_20220922_02_T1	2022-09-14	Landsat-8
LC08_L1TP_231077_20221101_20221108_02_T1	2022-11-01	Landsat-8
LC08_L1TP_231077_20230426_20230501_02_T1	2023-04-26	Landsat-8
LC08_L1TP_231077_20230629_20230711_02_T1	2023-06-29	Landsat-8
LC08_L1TP_231077_20230917_20230925_02_T1	2023-09-17	Landsat-8
LC08_L1TP_231077_20231206_20231209_02_T1	2023-12-06	Landsat-8
LC08_L1TP_231077_20240428_20240511_02_T1	2024-04-28	Landsat-8
LC08_L1TP_231077_20240717_20240723_02_T1	2024-07-17	Landsat-8
LC08_L1TP_231077_20241005_20241008_02_T1	2024-10-05	Landsat-8

Table S1. Landsat-8 scenes used in this study.

Scene ID	Acquisition Date	Instrument
S2B_MSIL1C_20170501T143729_N0500_R053_T20KKU	2017-05-01	Sentinel-2B
S2B_MSIL1C_20170610T143739_N0500_R053_T20KKU	2017-06-10	Sentinel-2B
S2B_MSIL1C_20170720T142749_N0500_R053_T20KKU	2017-07-20	Sentinel-2B
S2B_MSIL1C_20170829T142749_N0500_R053_T20KKU	2017-08-29	Sentinel-2B
S2B_MSIL1C_20171008T142739_N0500_R053_T20KKU	2017-10-08	Sentinel-2B
S2B_MSIL1C_20171117T142739_N0500_R053_T20KKU	2017-11-17	Sentinel-2B
S2B_MSIL1C_20180317T142849_N0500_R053_T20KKU	2018-03-17	Sentinel-2B
S2B_MSIL1C_20180526T143009_N0500_R053_T20KKU	2018-05-26	Sentinel-2B
S2B_MSIL1C_20180715T142849_N0500_R053_T20KKU	2018-07-15	Sentinel-2B
S2B_MSIL1C_20180903T142849_N0500_R053_T20KKU	2018-09-03	Sentinel-2B
S2B_MSIL1C_20181102T142849_N0500_R053_T20KKU	2018-11-02	Sentinel-2B
S2B_MSIL1C_20190322T142749_N0500_R053_T20KKU	2019-03-22	Sentinel-2B
S2B_MSIL1C_20190501T142759_N0500_R053_T20KKU	2019-05-01	Sentinel-2B
S2B_MSIL1C_20190620T142759_N0500_R053_T20KKU	2019-06-20	Sentinel-2B
S2B_MSIL1C_20190829T142759_N0500_R053_T20KKU	2019-08-29	Sentinel-2B
S2B_MSIL1C_20191028T142729_N0500_R053_T20KKU	2019-10-28	Sentinel-2B
S2B_MSIL1C_20200415T142729_N0500_R053_T20KKU	2020-04-15	Sentinel-2B
S2B_MSIL1C_20200803T142739_N0500_R053_T20KKU	2020-08-03	Sentinel-2B
S2B_MSIL1C_20201002T142739_N0500_R053_T20KKU	2020-10-02	Sentinel-2B
S2B_MSIL1C_20201101T142739_N0500_R053_T20KKU	2020-11-01	Sentinel-2B
S2B_MSIL1C_20210130T142729_N0500_R053_T20KKU	2021-01-30	Sentinel-2B
S2B_MSIL1C_20210410T142729_N0500_R053_T20KKU	2021-04-10	Sentinel-2B
S2B_MSIL1C_20210520T142729_N0500_R053_T20KKU	2021-05-20	Sentinel-2B
S2B_MSIL1C_20210629T142729_N0500_R053_T20KKU	2021-06-29	Sentinel-2B
S2B_MSIL1C_20210818T142729_N0500_R053_T20KKU	2021-08-18	Sentinel-2B
S2B_MSIL1C_20211017T142729_N0500_R053_T20KKU	2021-10-17	Sentinel-2B
S2B_MSIL1C_20220714T142719_N0510_R053_T20KKU	2022-07-14	Sentinel-2B
S2B_MSIL1C_20220813T142719_N0400_R053_T20KKU	2022-08-13	Sentinel-2B
S2B_MSIL1C_20220912T142719_N0400_R053_T20KKU	2022-09-12	Sentinel-2B
S2B_MSIL1C_20221101T142709_N0400_R053_T20KKU	2022-11-01	Sentinel-2B
S2B_MSIL1C_20230420T142719_N0509_R053_T20KKU	2023-04-20	Sentinel-2B
S2B_MSIL1C_20230619T142719_N0509_R053_T20KKU	2023-06-19	Sentinel-2B
S2B_MSIL1C_20230808T142719_N0509_R053_T20KKU	2023-08-08	Sentinel-2B
S2B_MSIL1C_20230917T142719_N0509_R053_T20KKU	2023-09-17	Sentinel-2B
S2B_MSIL1C_20231106T142719_N0509_R053_T20KKU	2023-11-06	Sentinel-2B
S2B_MSIL1C_20231206T142709_N0509_R053_T20KKU	2023-12-06	Sentinel-2B
S2B_MSIL1C_20240504T142719_N0510_R053_T20KKU	2024-05-04	Sentinel-2B
S2B_MSIL1C_20240623T142719_N0510_R053_T20KKU	2024-06-23	Sentinel-2B
S2B_MSIL1C_20240812T142719_N0511_R053_T20KKU	2024-08-12	Sentinel-2B
S2B_MSIL1C_20240911T142719_N0511_R053_T20KKU	2024-09-11	Sentinel-2B
S2B_MSIL1C_20241011T142709_N0511_R053_T20KKU	2024-10-11	Sentinel-2B

Table S2. Sentinel-2 scenes used in this study.

Scene ID	Acquisition Date	Instrument
20161010_134327_0e1f	2016-10-10	PS2
20161205_134509_0e1f	2016-12-05	PS2
20170103_134603_0e2f	2017-01-03	PS2
20170109_134606_0e1f	2017-01-09	PS2
20170130_134609_0e19	2017-01-30	PS2
20170304_134804_0e1f	2017-03-04	PS2
20170414_134154_1009	2017-04-14	PS2
20170427_134225_1038	2017-04-27	PS2
20170516_134250_1004	2017-05-16	PS2
20170609_134354_103b	2017-06-09	PS2
20170627_135050_0e20	2017-06-27	PS2
20170713_134644_102f	2017-07-13	PS2
20170815_134756_1039	2017-08-15	PS2
20170914_134857_1014	2017-09-14	PS2
20171010_135004_0f25	2017-10-10	PS2
20171102_135116_1033	2017-11-02	PS2
20171123_135151_1040	2017-11-23	PS2
20171212_135346_1022	2017-12-12	PS2
20171230_135322_1032	2017-12-30	PS2
20180209_135502_1015	2018-02-09	PS2
20180317_135624_0e0e	2018-03-17	PS2
20180326_135719_0f17	2018-03-26	PS2
20180410_135647_1002	2018-04-10	PS2
20180520_135909_102e	2018-05-20	PS2
20180608_135940_1032	2018-06-08	PS2
20180704_140009_100c	2018-07-04	PS2
20180908_135855_0e0e	2018-09-08	PS2
20181001_140308_0f35	2018-10-01	PS2
20181122_140509_1044	2018-11-22	PS2
20181211_140507_1010	2018-12-11	PS2
20190122_140653_101f	2019-01-22	PS2
20190211_140615_1014	2019-02-11	PS2
20190221_140831_100a	2019-02-21	PS2
20190306_140811_1034	2019-03-06	PS2
20190513_140914_0f22	2019-05-13	PS2
20190626_140959_103c	2019-06-26	PS2
20190803_140219_0e0f	2019-08-03	PS2
20191007_140308_0e0f	2019-10-07	PS2
20191129_141216_0f35	2019-11-29	PS2
20200108_141305_103d	2020-01-08	PS2
20200311_141242_1014	2020-03-11	PS2
20200415_141329_1006	2020-04-15	PS2
20200629_141348_0f28	2020-06-29	PS2

Table S3. PlanetScope scenes from the older Dove-C (PS2) generation that were used in this study.

Scene ID	Acquisition Date	Instrument
20200328_134314_64_2263	2020-03-28	PSB.SD
20200516_134707_21_2277	2020-05-16	PSB.SD
20200729_134905_10_2277	2020-07-29	PSB.SD
20200905_134846_16_222b	2020-09-05	PSB.SD
20200909_143842_94_227a	2020-09-09	PSB.SD
20201005_135131_66_2277	2020-10-05	PSB.SD
20201128_135312_33_2259	2020-11-28	PSB.SD
20210316_134737_82_241e	2021-03-16	PSB.SD
20210420_134520_10_242d	2021-04-20	PSB.SD
20210531_134614_85_241e	2021-05-31	PSB.SD
20210603_134145_29_2456	2021-06-03	PSB.SD
20210612_134245_50_2456	2021-06-12	PSB.SD
20210710_134242_08_2465	2021-07-10	PSB.SD
20210815_143231_23_2426	2021-08-15	PSB.SD
20210926_142938_21_2274	2021-09-26	PSB.SD
20211127_133936_00_2455	2021-11-27	PSB.SD
20220323_140918_59_2485	2022-03-23	PSB.SD
20220403_133912_23_2435	2022-04-03	PSB.SD
20220505_133805_86_242b	2022-05-05	PSB.SD
20220602_135219_78_2251	2022-06-02	PSB.SD
20220619_141044_55_24a4	2022-06-19	PSB.SD
20220823_133629_45_2465	2022-08-23	PSB.SD
20220827_142307_95_2274	2022-08-27	PSB.SD
20220915_141739_37_227b	2022-09-15	PSB.SD
20220920_133236_87_241b	2022-09-20	PSB.SD
20221101_140857_70_2490	2022-11-01	PSB.SD
20221125_135421_91_2262	2022-11-25	PSB.SD
20221227_140803_96_247d	2022-12-27	PSB.SD
20230120_133456_89_2465	2023-01-20	PSB.SD
20230220_132456_32_2445	2023-02-20	PSB.SD
20230425_141309_40_247b	2023-04-25	PSB.SD
20230428_141134_83_2481	2023-04-28	PSB.SD
20230521_134150_77_24a8	2023-05-21	PSB.SD
20230619_141547_48_2482	2023-06-19	PSB.SD
20230715_141834_80_2438	2023-07-15	PSB.SD
20230902_134031_65_2431	2023-09-02	PSB.SD
20231014_142115_34_247f	2023-10-14	PSB.SD
20240324_143040_50_227a	2024-03-24	PSB.SD
20240419_143924_29_24e0	2024-04-19	PSB.SD
20240421_144040_52_24f9	2024-04-21	PSB.SD
20240619_135343_79_24c8	2024-06-19	PSB.SD
20240712_143924_94_24e1	2024-07-12	PSB.SD
20240807_135345_66_2417	2024-08-07	PSB.SD
20241001_144352_41_24cd	2024-10-01	PSB.SD

Table S4. PlanetScope scenes from the newer SuperDove (PSB.SD) generation that were used in this study.

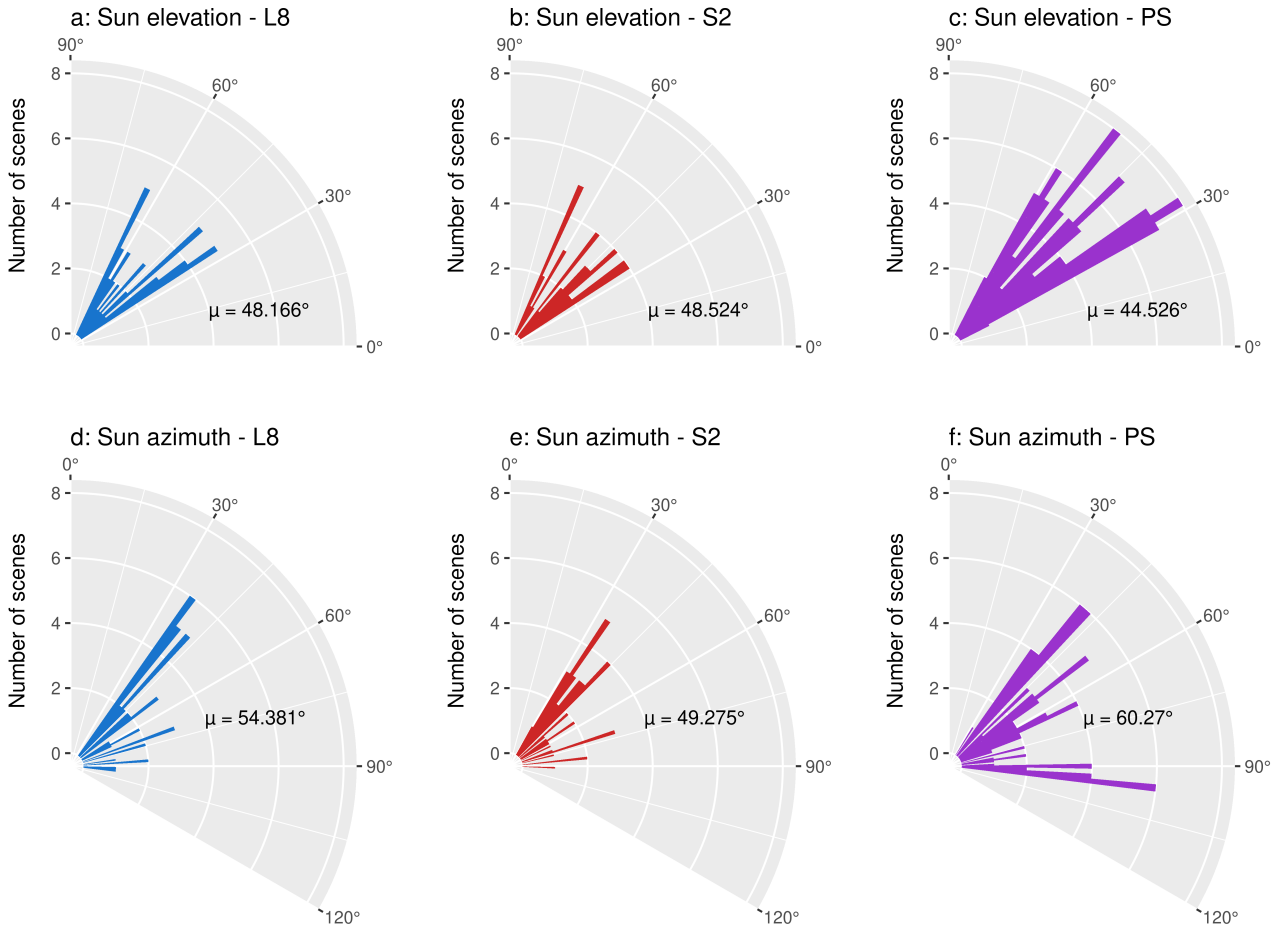

Figure S2. Distribution of sun elevation (a–c) and azimuth angle (d–f) of all scenes used in this study plotted separately for each satellite.

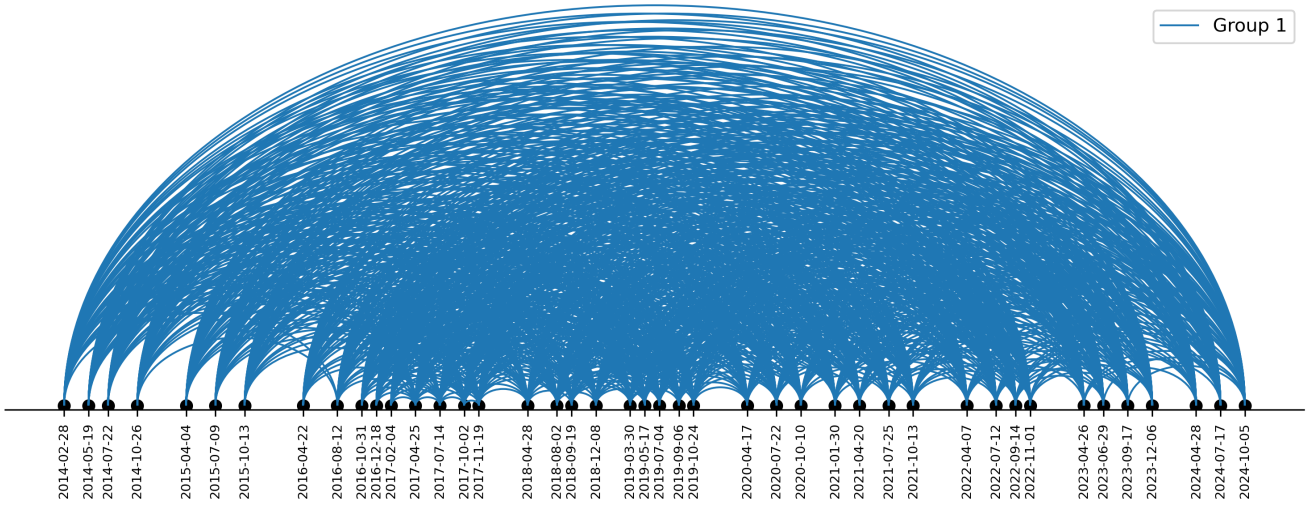

Figure S3. Correlation network of the Landsat-8 scenes used in this work, comprising a total of 785 connections.

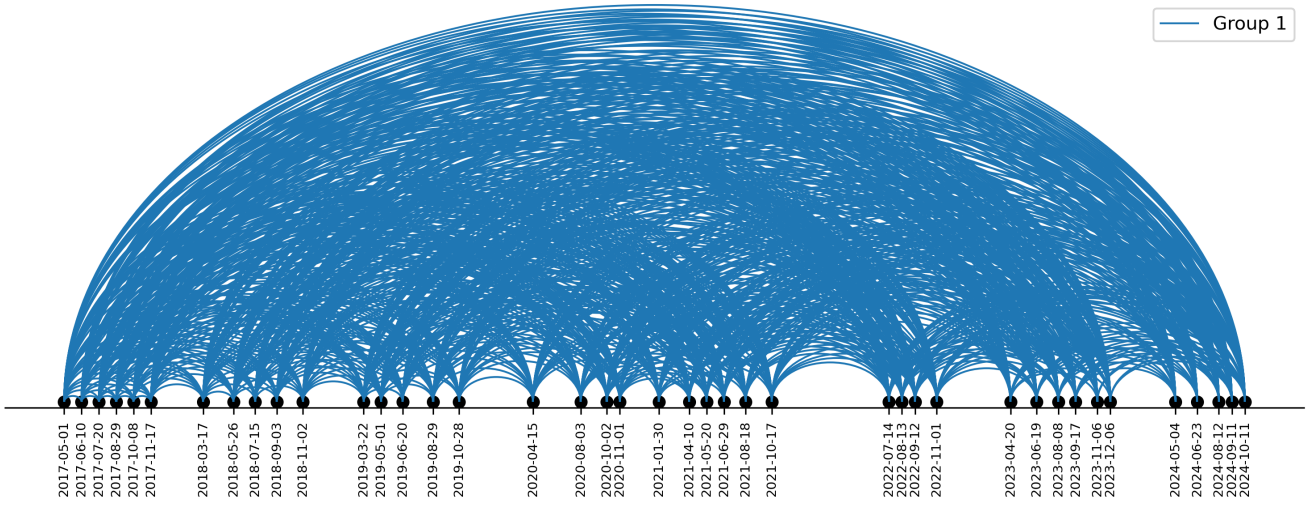

Figure S4. Correlation network of the Sentinel-2 scenes used in this work, comprising a total of 716 connections.

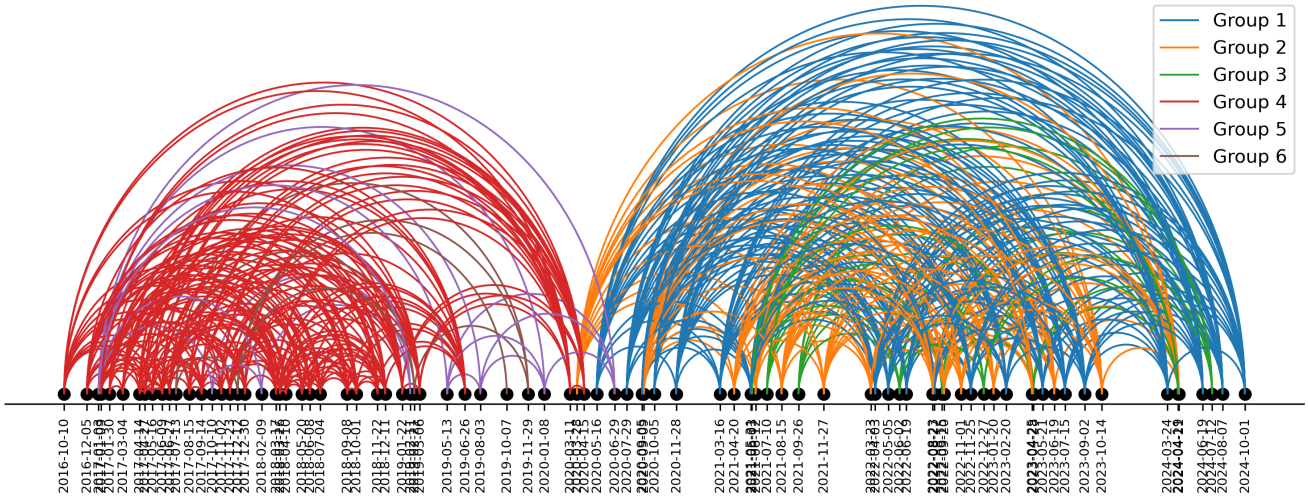

Figure S5. Correlation network of the PlanetScope scenes used in this work. Through restricting image pairs to a common instrument generation (PS2 and PSB.SD) and similar satellite view angle to reduce orthorectification errors, we obtain a disconnected network with a total of 491 correlation pairs from 6 distinct groups.

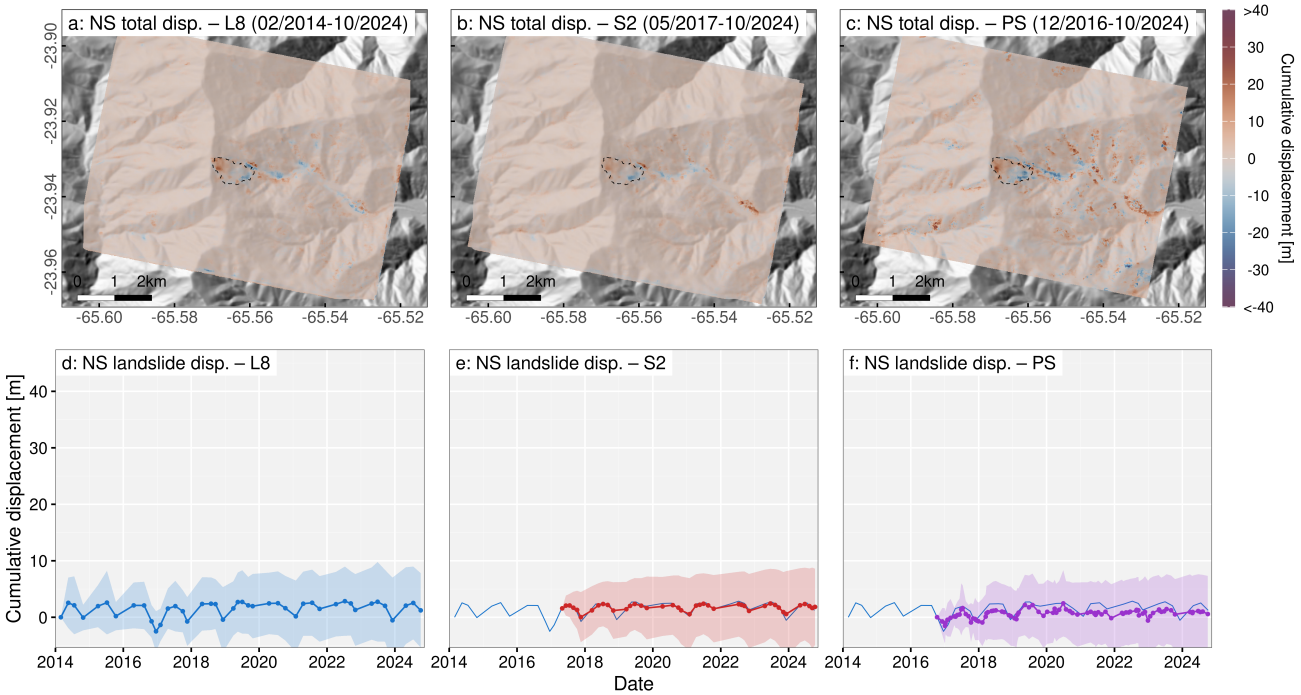

Figure S6. Map view of the total cumulative displacement estimated at each pixel after inversion for Landsat-8 (a), Sentinel-2 (b), and PlanetScope (c) networks over the respective time span covered by the available satellite data. The plots show the north-south (NS) component, which is largely unaffected by the landslide motion due to its eastward aspect. Plots (d) to (f) show the mean and standard deviation (ribbon) of the cumulative displacement estimated over the landslide surface (see dashed polygon in a-c) for all three data sets. While the cumulative displacement remains close to zero, a clear seasonal oscillation bias pattern is visible.

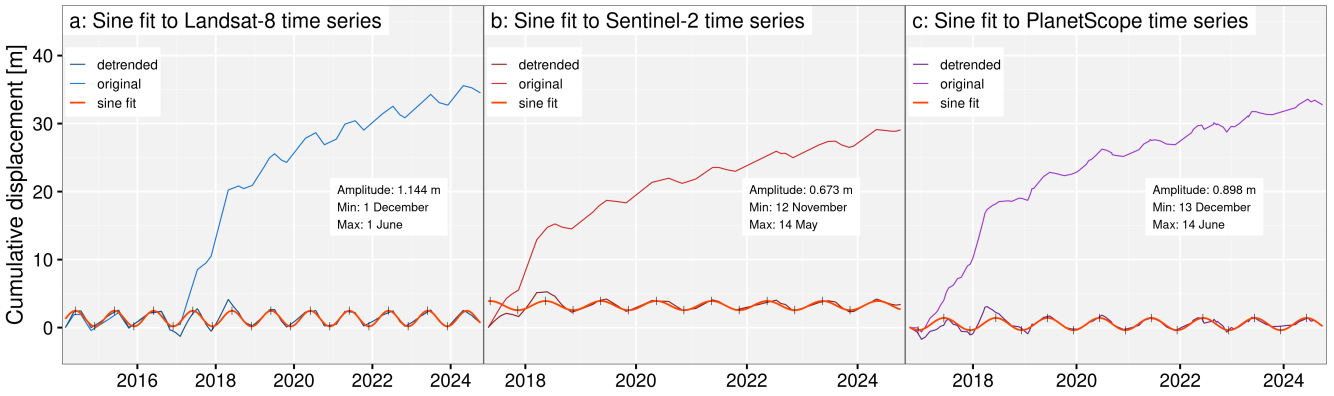

Figure S7. Example of modeling of the seasonal oscillation signal for the mean displacement time series of Landsat-8 (a), Sentinel-2 (b), and PlanetScope (c) obtained over the Del Medio landslide through a sinusoidal fit. We show the original and detrended displacement time series together with the fitted sine wave and the parameters of the estimated fit.

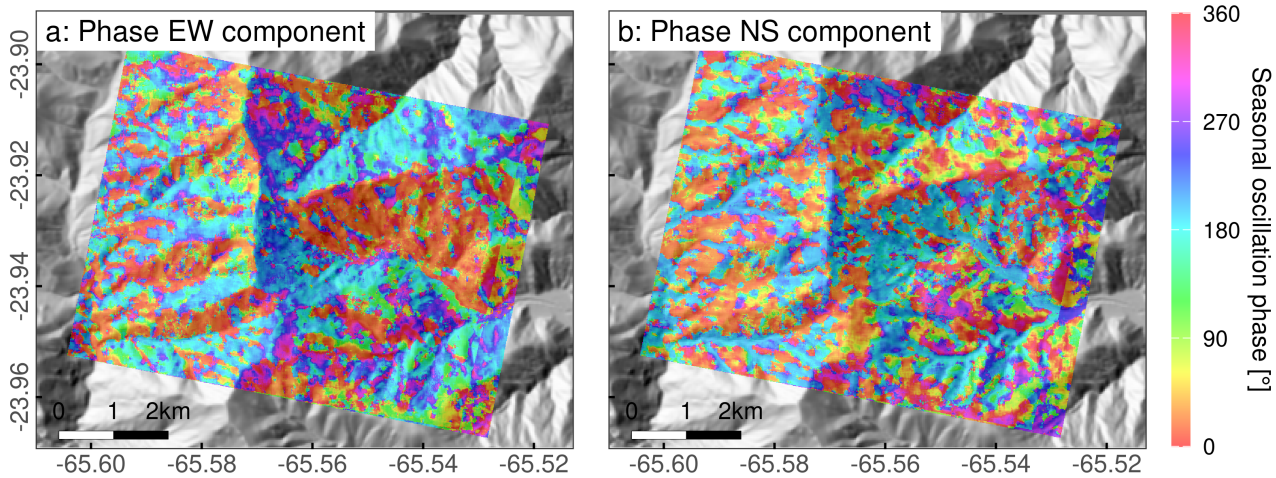

Figure S8. Estimated phase of the seasonal oscillation in the PlanetScope inversion results for the east-west (EW) (a) and north-south (NS) (b) component. The phase was estimated by removing the long-term trend from the displacement signal and fitting a sine with a one-year wavelength.

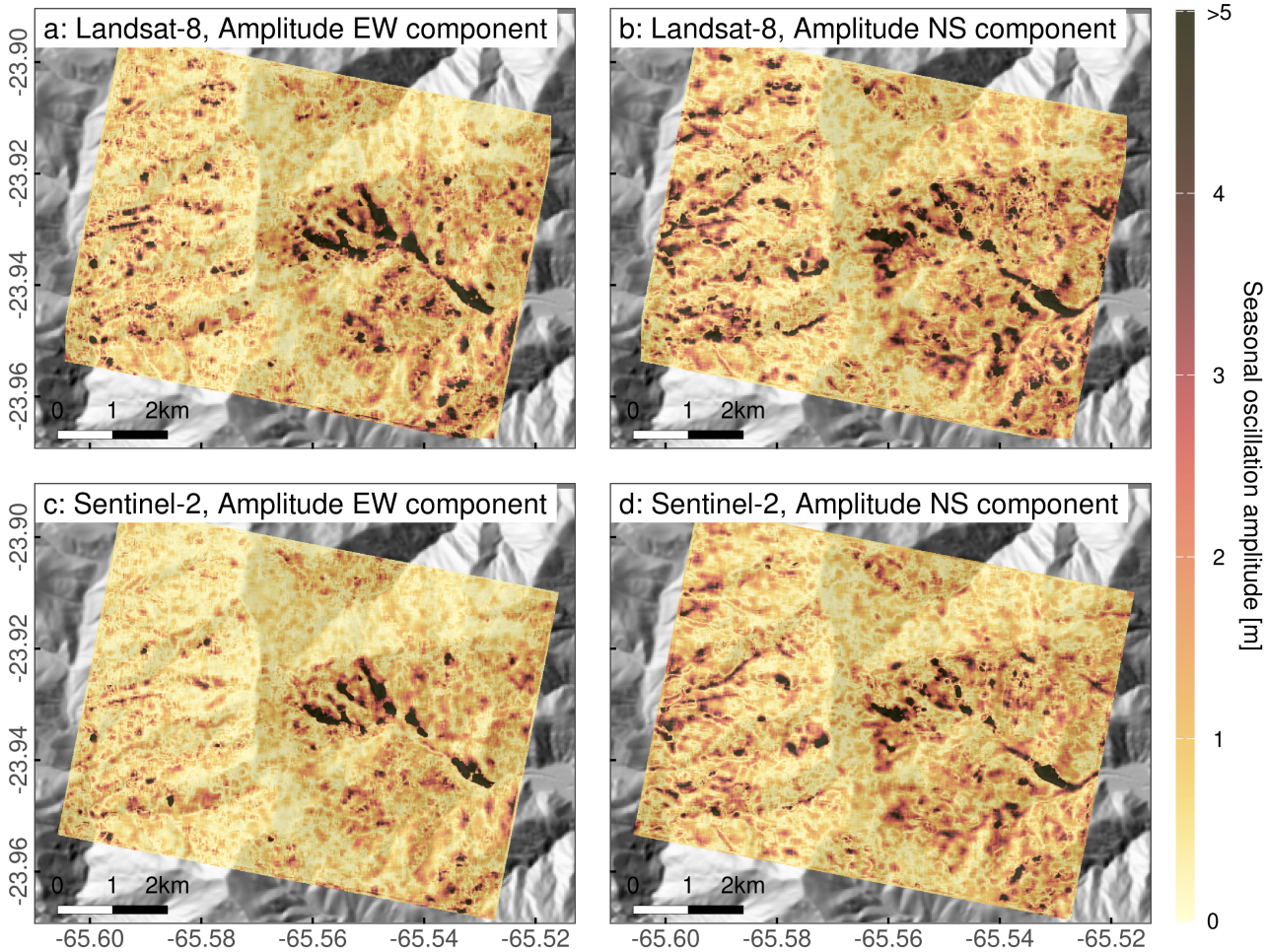

Figure S9. Amplitude of the seasonal oscillation in the Landsat-8 (a, b) and Sentinel 2 (c, d) inversion results for the east-west (EW) (a, c) and north-south (NS) (b, d) component. The amplitude was estimated by removing the long-term trend from the displacement signal and fitting a sine with a one-year wavelength.

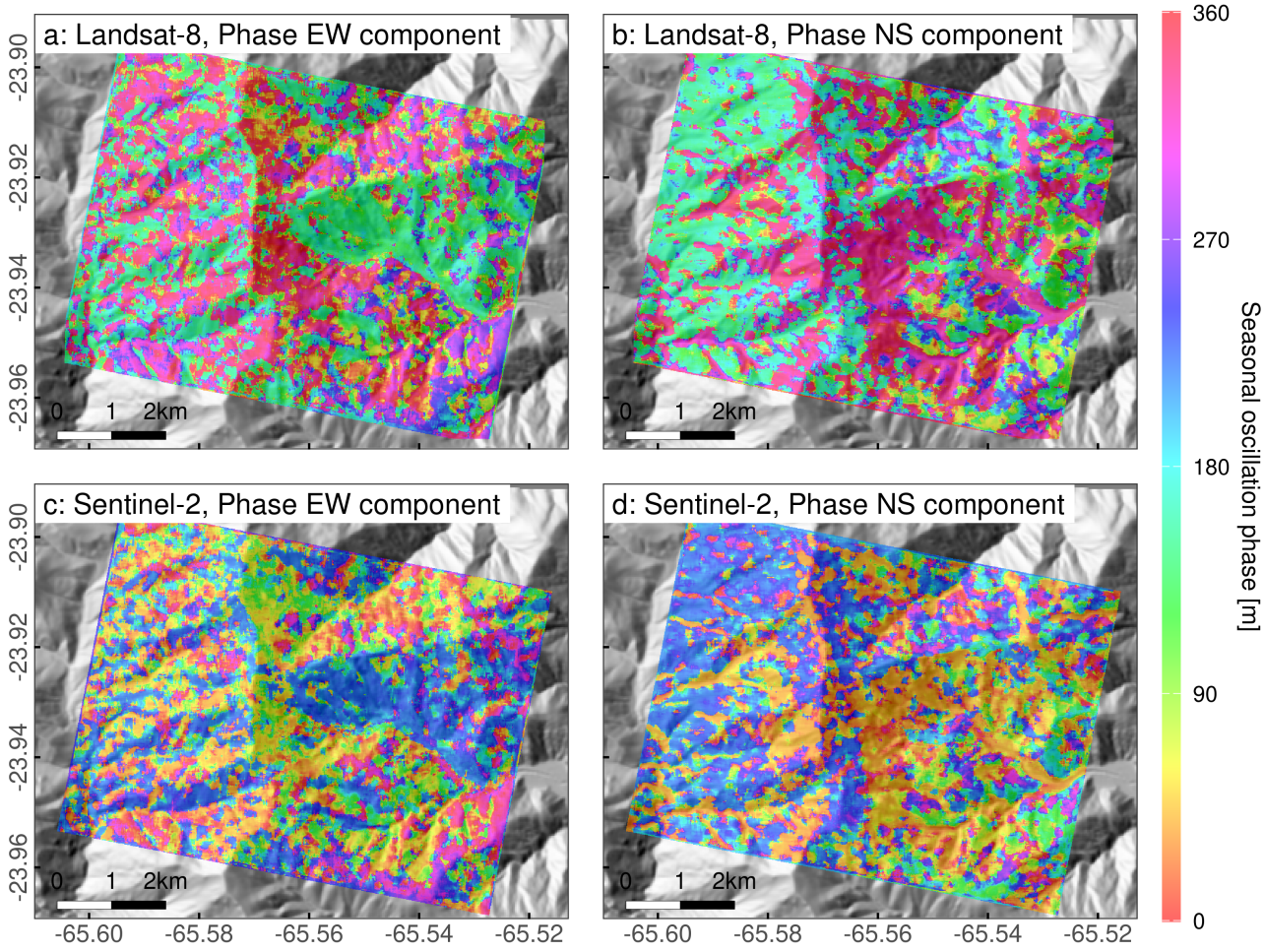

Figure S10. Estimated phase of the seasonal oscillation in the Landsat-8 (a, b) and Sentinel 2 (c, d) inversion results for the east-west (EW) (a, c) and north-south (NS) (b, d) component. The phase was estimated by removing the long-term trend from the displacement signal and fitting a sine with a one-year wavelength.

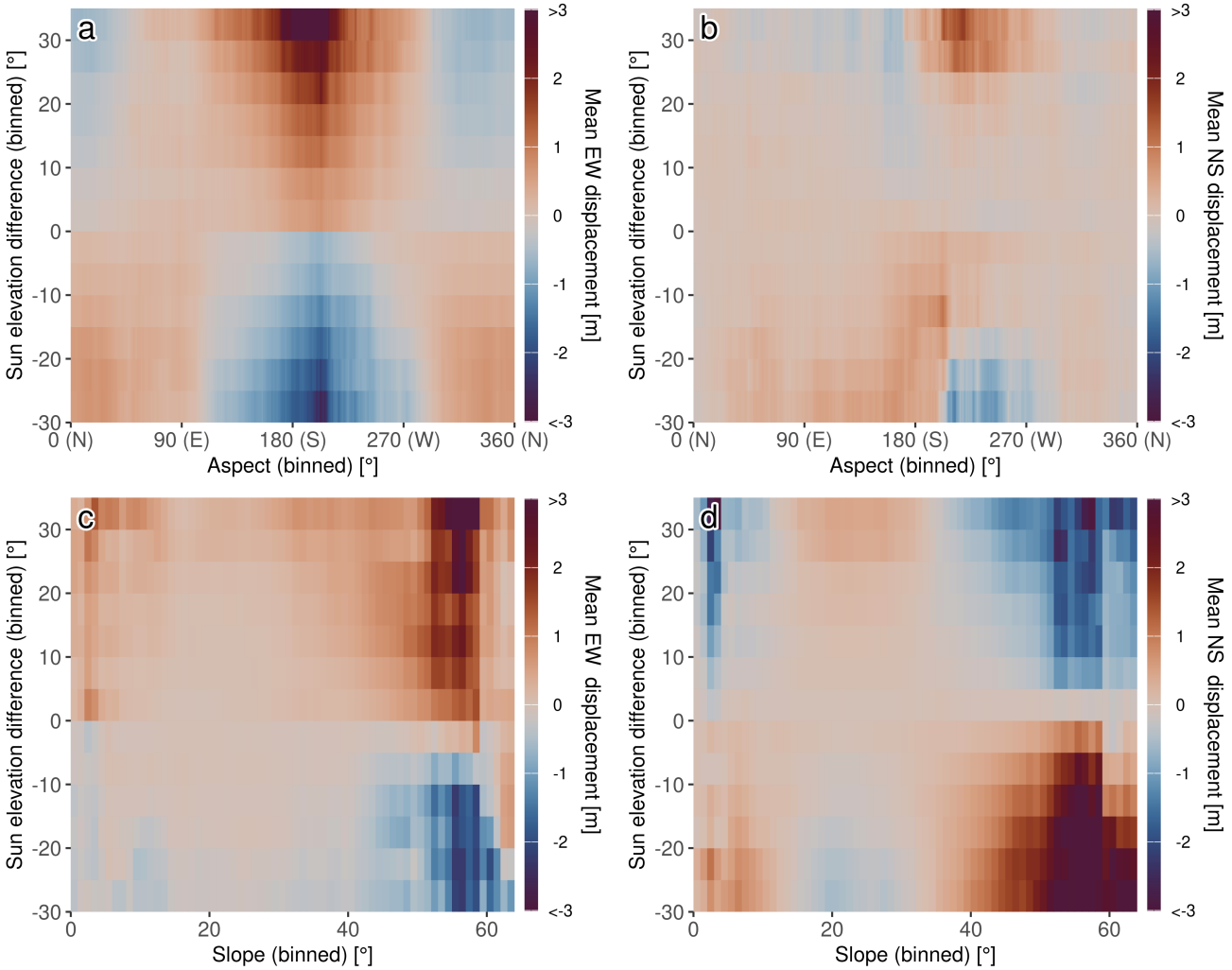

Figure S11. Mean displacement estimated over stable terrain in all 491 displacement maps retrieved from PlanetScope imagery. We binned pixels according to the sun elevation difference between the correlated image pair (5-degree bins) and the terrain aspect (a, b) and slope (c, d), both in 1-degree bins. While over stable terrain, the displacement is expected to be zero, we can observe a systematic error depending on the terrain aspect at high sun elevation differences. This relation also has a dependence on terrain slope. These measurement errors are the basis for the subsequent oscillation pattern when the network is inverted.

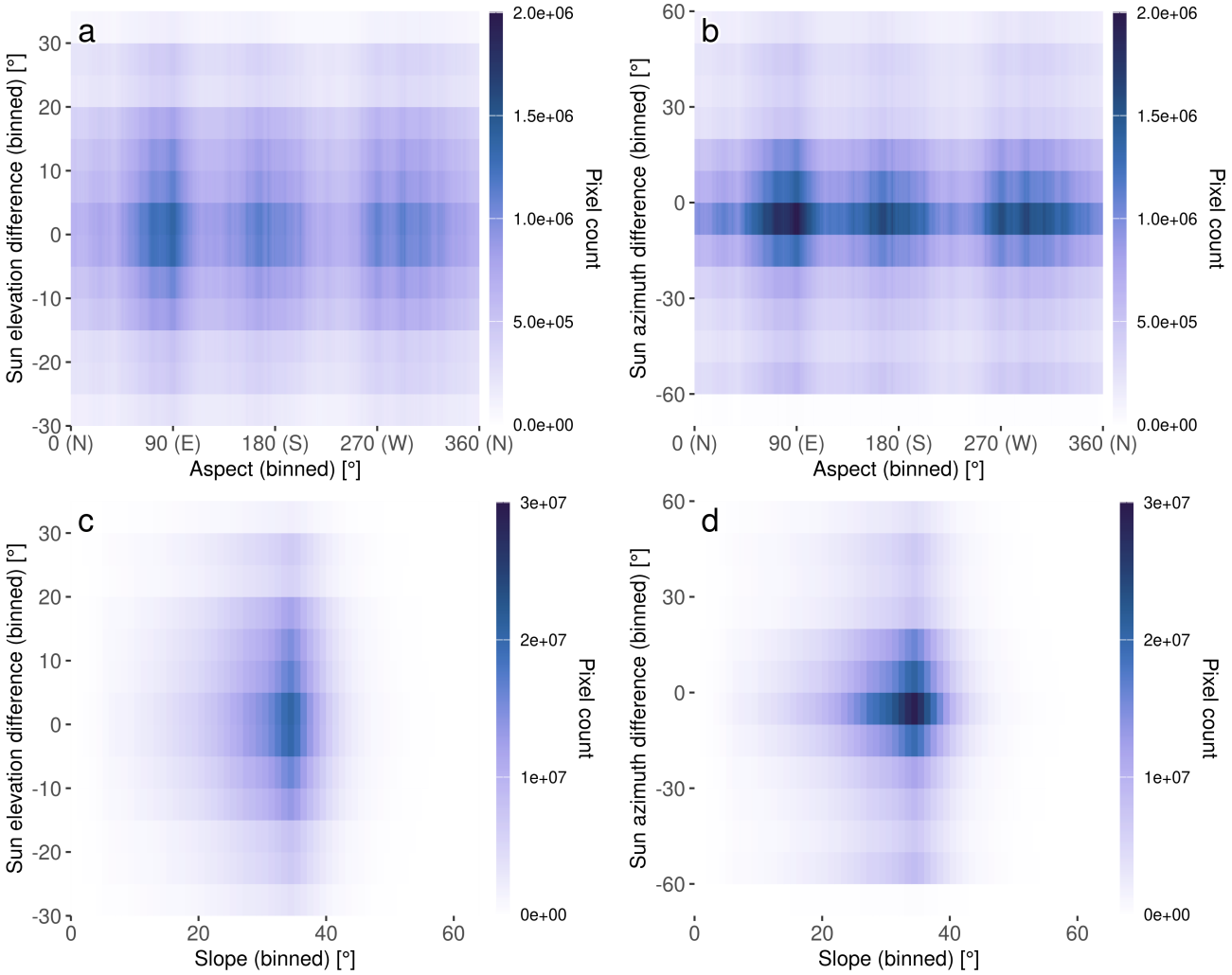

Figure S12. Pixel count associated with the binned displacement error plots (main manuscript, Figure 4, Figure S11) for bins of aspect (a, b), slope (c, d), sun elevation difference (a, c) and sun azimuth difference (b, d).

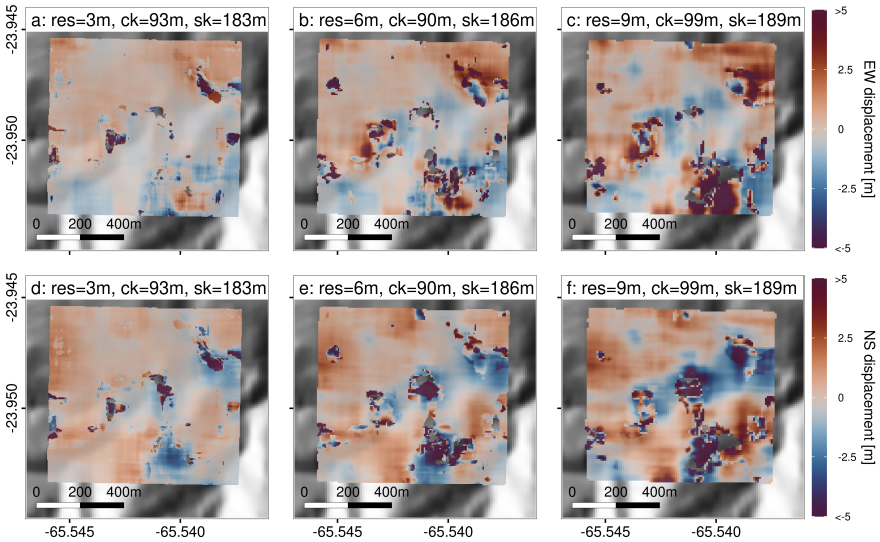

Figure S13. Displacement estimated from a PlanetScope image pair (16.05.2020 and 05.09.2020) in east-west (EW) (a–c) and north-south (NS) (d–f) direction over a small sample area of stable terrain. The plot illustrates the seasonal bias at different resolutions, analog to plot 5 in the main manuscript, but using parabola fitting (subpixel mode 1) for the subpixel refinement.

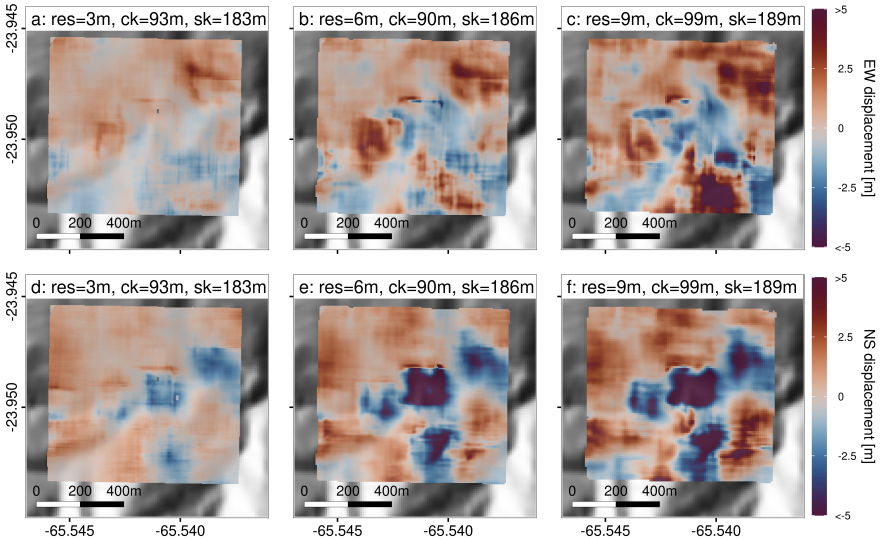

Figure S14. Displacement estimated from a PlanetScope image pair (16.05.2020 and 05.09.2020) in east-west (EW) (a–c) and north-south (NS) (d–f) direction over a small sample area of stable terrain. The plot illustrates the seasonal bias at different resolutions, analog to plot 5 in the main manuscript, but using the simple affine correlator (subpixel mode 3) for the subpixel refinement.

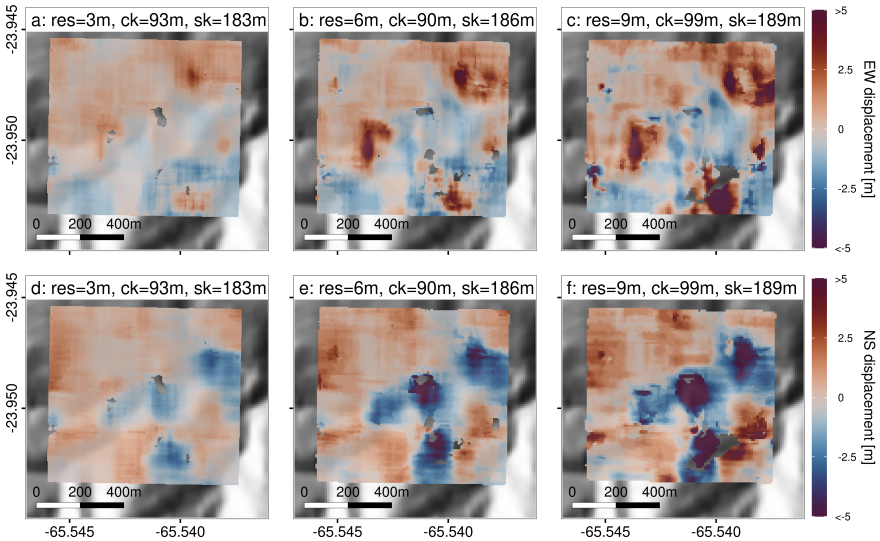

Figure S15. Displacement estimated from a PlanetScope image pair (16.05.2020 and 05.09.2020) in east-west (EW) (a–c) and north-south (NS) (d–f) direction over a small sample area of stable terrain. The plot illustrates the seasonal bias at different resolutions, analog to plot 5 in the main manuscript, but using phase correlation (subpixel mode 4) for the subpixel refinement.

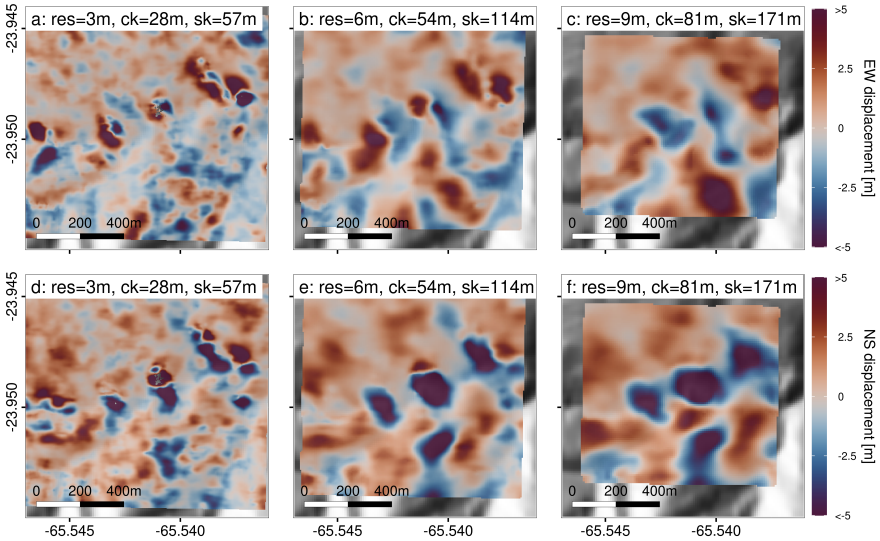

Figure S16. Displacement estimated from a PlanetScope image pair (16.05.2020 and 05.09.2020) in east-west (EW) (a–c) and north-south (NS) (d–f) direction over a small sample area of stable terrain. The plot illustrates the seasonal bias at different resolutions, analog to plot 5 in the main manuscript, but using a different correlation algorithm (more global matching). As the maximum correlation kernel size for this algorithm is 9x9 pixel, the kernel size could not be kept constant considering the spatial resolution of the input images.

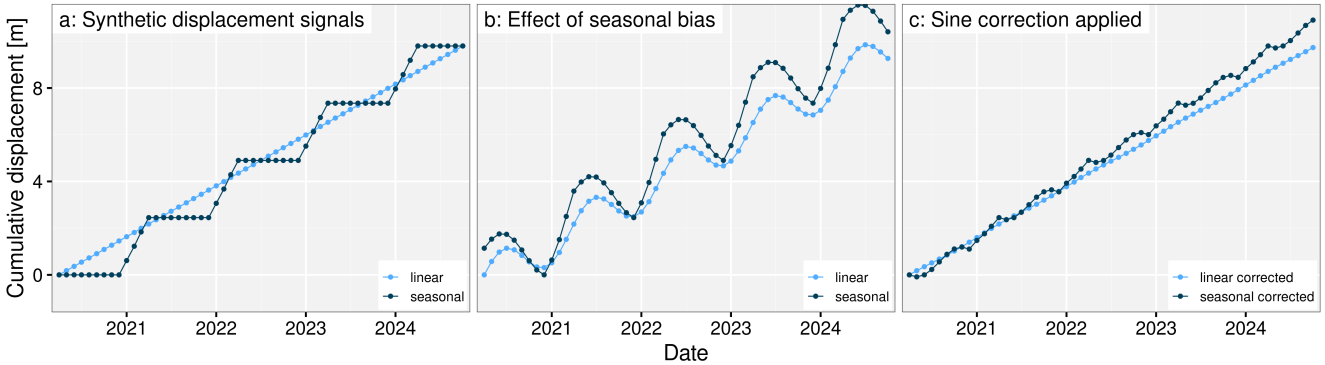

Figure S17. (a) Example of how a displacement time series of a seasonally driven landslide (dark blue) could look in comparison to a purely linear signal (light blue). When these synthetic displacement signals are affected by seasonal bias (b), it becomes difficult to distinguish between the actual displacement signal and the seasonal oscillation bias. Applying a sine correction to both time series (c), may over-correct any true seasonal response signal. Displacement magnitudes and seasonal oscillation bias are modeled after the displacement estimated for the period between 2020 and 2024, which showed relatively uniform displacement.

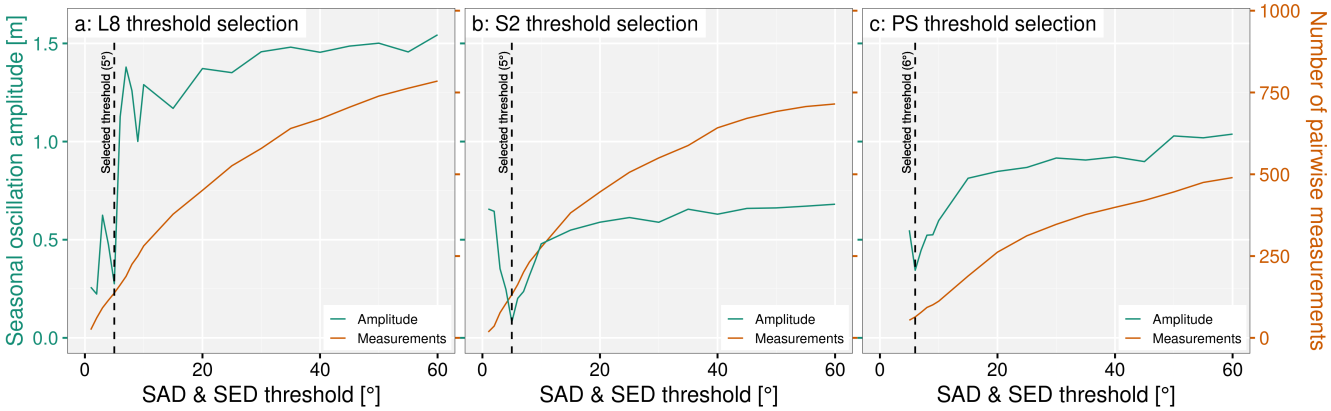

Figure S18. Seasonal oscillation amplitude estimated over the Del Medio landslide and number of available image pairs for different sun-azimuth and sun-elevation difference (SAD, SED) thresholds. We selected the threshold that maximized the number of pairwise measurements in a network while minimizing the seasonality in the resulting time series. This was 5 degrees for Landsat-8 (a) and Sentinel-2 (b), and 6 degrees for PlanetScope.

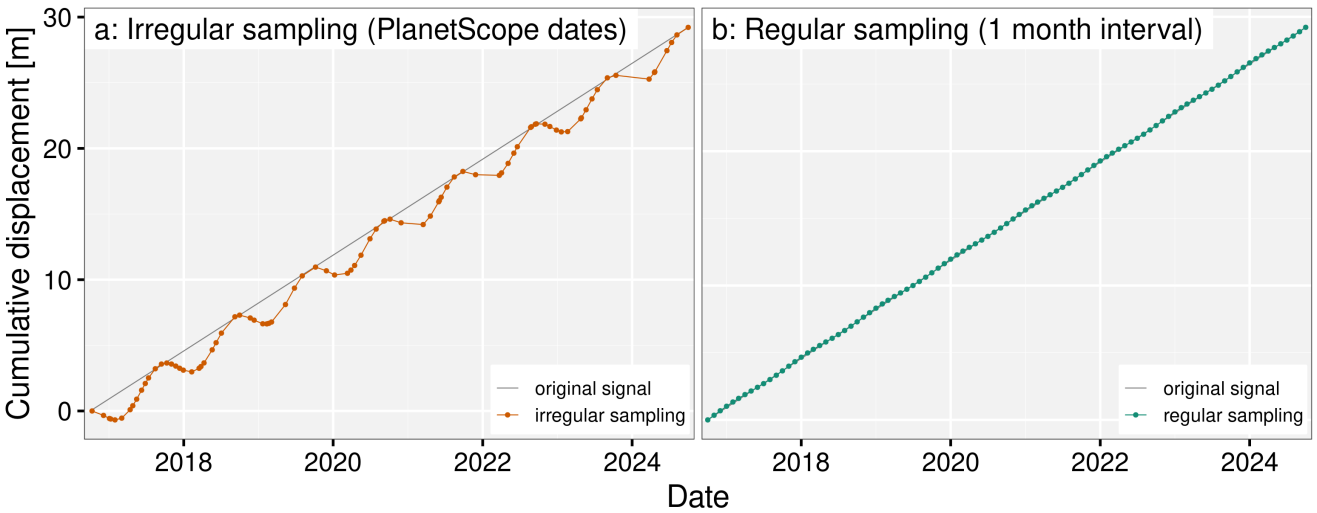

Figure S19. Time-series inversion results based on a synthetic linear displacement signal. We have sampled the signal to create two different artificial networks, one with acquisition dates based on the PlanetScope scenes used in this study (irregular) and one with a regular sampling interval of one month. When seasonal bias is added to the pairwise measurements in the network, the inversion results of the irregular network show the familiar seasonal oscillation pattern (a). The regular network, however, is only marginally affected, as positive and negative measurement errors are evenly distributed and cancel each other out in the inversion process (b).

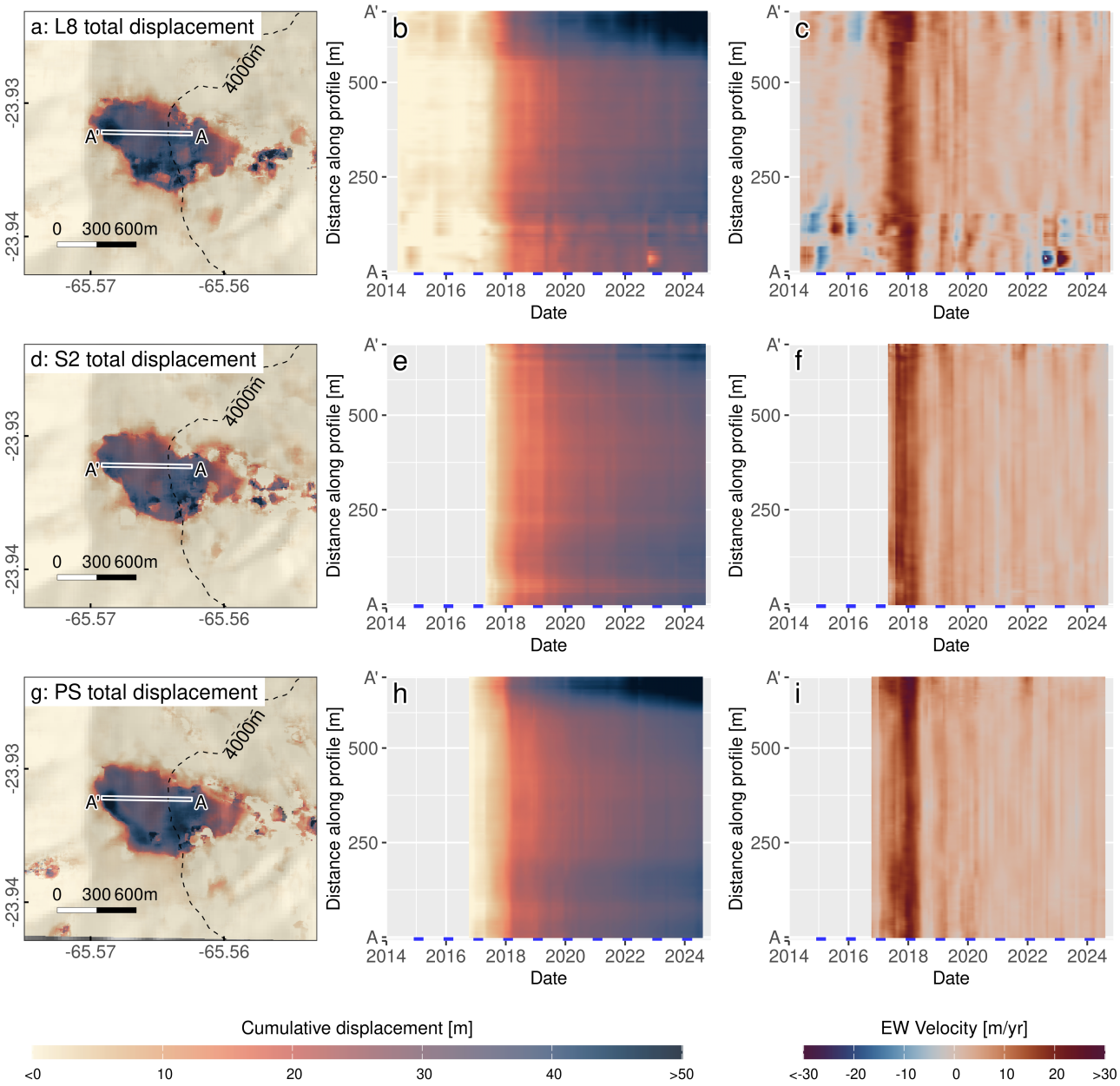

Figure S20. Spatially variable displacement rates along a profile over the Del Medio landslide. The maps in the first column show the total displacement estimated over the landslide throughout the observation period, the location of the profile, and the 4000 m contour line for Landsat-8 (a), Sentinel-2 (d), and PlanetScope (g). The cumulative displacement through time along this profile is plotted in the second column for the respective satellites. To better identify periods of acceleration, we derived the velocity from the smoothed (rolling mean with a half-year window) cumulative displacement, as shown in Figures c, f, and i. For both the second and third columns, we indicate the monsoon season (December - March) with blue bars along the x-axis. Seasonal bias was compensated using image pairs with similar illumination for the inversion only.

References

Mueting, A. and Bookhagen, B.: Tracking slow-moving landslides with PlanetScope data: new perspectives on the satellite's perspective, EGUsphere, 2023, 1–36, https://doi.org/10.5194/egusphere-2023-1698, 2023.